Probing the basement of southern Tibet: evidence from crustal xenoliths entrained in a Miocene ultrapotassic dyke

G. H.-N. Chan[1,5]
D. J. Waters[1], *
M. P. Searle[1]
J. C. Aitchison[2]
M. S. A. Horstwood[3]
Q. Crowley[3]
C.-H. Lo[4]
J. S.-L. Chan[2]
[1]Department of Earth Sciences, Parks Road, Oxford University, OX1 3PR, UK
[2]Department of Earth Sciences, University of Hong Kong, Hong Kong
[3]NERC Isotope Geosciences Laboratory, Keyworth, Nottingham, NG12 5GG, UK.
[4]Department of Geosciences, National Taiwan University, Taipei, Taiwan
[5]SRK Consulting, 10 Richardson Street, West Perth, 6005 WA, Australia

*E-mail: dave.waters@earth.ox.ac.uk

197 words in the abstract, 3004 words in the main text and acknowledgment, 3 figures, 6 tables & 39 references

ABSTRACT

A variety of felsic and mafic granulites and ultramafic rocks occur as xenoliths within a 12.7-million-year-old ultrapotassic dyke intruding Xigaze flysch immediately to the north of the Yarlung-Tsangpo suture zone in southern Tibet. Garnet-clinopyroxene-plagioclase-quartz thermobarometry on mafic granulite xenoliths gives temperatures of 1130-1330 °C and pressures between 22-26 kbar indicating equilibration in the high-pressure and ultrahigh-temperature granulite field and defining a geotherm of ca. 16 °C/km. Ultramafic xenoliths consist mainly of hornblende and biotite, probably of restitic crustal rather than mantle origin, and attained peak metamorphic conditions of 920-1130 °C and 17-24 kbar, whereas felsic granulites equilibrated at 870-900 °C at an inferred pressure of 17 kbar. *In-situ* U-(Th)-Pb LA-ICP-MS dating of zircons shows that protoliths may include Proterozoic basement rocks, Late Cretaceous calc-alkaline tonalites of the Gangdese batholith root and/or remnants of a Neo-Tethyan oceanic arc. Certain zircons from a felsic granulite and an ultramafic xenolith have mean $^{206}Pb/^{238}U$ ages of 16.8 ± 0.9 and 15.6 ± 0.6 Ma respectively, and monazites from a micaceous xenolith yielded a mean $^{208}Pb/^{232}Th$ age of 14.4 ± 0.4 Ma. These results show that the southern Tibet basement reached ca. 80 km thickness by 17-14 Ma at the latest and that the crust remained as thick to the present day.

The double thickness (70-80 km) crust of southern Tibet (Owens & Zandt 1997; Schulte-Pelkum et al. 2005) includes the northern Tethyan Himalaya (Indian plate), Yarlung-Tsangpo suture zone and southern Lhasa terrane (Asian plate). Seismic imaging during the INDEPTH project (Nelson et al. 1996; Hauck et al. 1998) shows that the Tethyan Himalayan rocks thicken toward to the north, along with the northward underthrusting Greater Himalayan wedge. Moho depth deepens from 35 km under the southern margin of the Himalaya to ca. 70-80 km thick beneath southern Tibet (Schulte-Pelkum et al. 2005). Upper mantle seismic velocities show that cold and strong upper mantle occurs beneath south Tibet whereas hot and weak mantle occurs beneath north of ca. 32 °N near the position of Bangong suture zone (Tilmann et al. 2003) (Fig. 1a).

Studies of lower crustal and upper mantle xenoliths play an important role in the understanding of the thickening history of the Tibetan plateau and have implications for models of plateau uplift and the Himalayan belt formation. Lower crustal xenolith- localities have been reported in different areas of Tibet (Hacker et al. 2000, 2005; Ducea et al. 2003; Jolivet et al. 2003; Ding et al. 2007), but until now, no lower crustal xenoliths have been recovered from southern Tibet. In this paper we describe some rare lower crustal xenoliths collected from an ultrapotassic dyke intruding the Xigaze flysch immediately north of the Yarlung-Tsangpo suture zone (Fig. 1b). We infer depth of origin from thermobarometry, and age of protolith and timing of granulite facies metamorphism of the xenoliths from U-(Th-)Pb dating of zircons and monazites. We use these data to determine the thermal state of the Lhasa terrane lower crust at the time of the xenolith recrystallization and speculate on the structural evolution of the south Tibet lower crust with time.

SOUTHERN TIBET CRUSTAL XENOLITH SAMPLES

The northwest-southeast trending xenolith-bearing dike intrudes the Xigaze flysch, 20 km west of Ngamring in southern Tibet (29°19'50.05", 87°0'39.17"; Fig. 1b). It is andesitic (SiO_2 = 56.1 wt%) and ultrapotassic (K_2O/Na_2O = 7.7; K_2O = 5.7 wt%) with a high concentration of incompatible trace elements (e.g. Rb = 340 ppm). Petrographically, biotite and potassium feldspar phenocrysts are set in a microcrystalline matrix of potassium feldspar, biotite, quartz, titaniferous magnetite and glass. The entrained xenoliths range in size from 5-100 mm, including diopside marble, quartzite, felsic and mafic granulite plus ultramafic xenoliths. The felsic granulites consist of quartz + plagioclase + potassium feldspar + garnet + rutile + apatite + zircon ± biotite, whereas the mafic granulites comprise plagioclase + clinopyroxene + garnet + quartz + amphibole + rutile + apatite ± biotite ± zircon. The ultramafic xenoliths consist of clinopyroxene + garnet + amphibole + biotite + titanite + rutile + apatite ± plagioclase ± pyrite ± zircon. In addition, a rare micaceous xenolith dominated by biotite with trace amounts of garnet, rutile, apatite, zircon and monazite was also found.

All meta-igneous xenoliths are granoblastic except for the micaceous xenolith which is foliated. Most of the mafic granulites and ultramafic xenoliths exhibit secondary textures including the breakdown of primary sodic clinopyroxene to plagioclase + low-Na clinopyroxene symplectite and formation of tens of micrometers thick rinds of kelyphite surrounding garnets. These kelyphites are interpreted to have formed during decompression in a H_2O undersaturated environment (O'Brien & Rotzler 2003). Textures in the micaceous xenolith demonstrate that it has been extensively modified, probably during its ascent to the surface in the magma. Textures include formation of quenched melt pockets; dehydration melting of biotite to form potassium feldspar + spinel; growth of new fine-grained biotite + potassium feldspar + quartz + apatite + titaniferous magnetite. These new phases also form the kelyphitic coronae around embayed garnets.

Mineral compositions (Table 1) and backscattered electron (BSE) images were acquired at Oxford University with a JEOL JXA8800R electron microprobe equipped with four wavelength spectrometers and a JEOL JSM-840A scanning electron microscope equipped with an Oxford Instruments Isis 300 energy-dispersive analytical system. Operating conditions were 10-20s counting time on each element peak, 20kV accelerating voltage, 40nA beam current (microprobe), and 100s live counting time, 20kV accelerating voltage and 6nA beam current (SEM). Both instruments were calibrated with the same set of standards and the ZAF correction procedure was used. Thermobarometry was determined using conventional thermometers (Powell 1985; Fuhrman & Lindsley 1988; Holdaway 2000) in combination with THERMOCALC 3.25 in average P mode (Powell and Holland, 1998). Results of individual samples and employed geothermobarometers are presented in Table 2 and plotted in Fig 2. The lack of zoning and restricted occurrence of retrograde minerals at rims indicate that the major phases in the xenoliths are well equilibrated, and the rocks experienced fast cooling and decompression with rapid exhumation to the surface. Heating of the xenoliths during their entrainment in the magma is a possibility; however, the temperature estimations reported here are unlikely to reflect this transient event given the short timescales and slow rate of volume diffusion of garnet and pyroxene (Hacker et al. 2005). The mafic granulites have the ideal mineral assemblage of Grt+Cpx+Plag+Qtz for thermobarometry. Application of the Grt-Cpx Fe-Mg exchange thermometer (Powell 1985) coupled with THERMOCALC 3.25 in average P mode reveals that sample 158f and 158o recrystallized at conditions of 1330 ± 50 °C, 25.8 ± 1.9 kbar and 1130 ± 50 °C, 21.9 ± 0.9 kbar respectively. Using the same combination of geothermobarometers, the ultramafic xenolith (158m) is estimated to have reached equilibrium at lower conditions of 920 ± 50 °C and 17.4 ± 1.0 kbar. These three samples define a linear array that corresponds to a geothermal gradient of ca. 16°C/km. Grt-Cpx thermometry on another ultramafic xenolith (158p) yields an equilibrium temperature of 1100-1130 ºC, but quantitative barometry cannot be performed on this sample as both plagioclase and quartz are absent. If all the samples are assumed to have been extracted along the same geotherm, an equilibrium pressure of 19-24 kbar can be estimated for 158p. By the same logic, the felsic granulite 158g equilibrated at 15-20 kbar with the temperature determined as 870-900 °C from coexisting ternary feldspars (Fuhrman & Lindsley 1988), while the micaceous xenolith records an Fe-Mg exchange temperature of 740-755 °C calculated with the Grt-Bt geothermometer of Holdaway (2000, calibration 5AV) at an assumed pressure of 13-17 kbar. Bulk rock composition estimated by combining mineral modes from backscattered electron image measurements with microprobe analyses (Table 3) suggests that the mafic and felsic granulites are derived from calc-alkaline tonalitic and granitic crust. The ultramafic xenoliths are rich in hornblende and biotite, have Mg# of 43.6-48.1 and contain 15.4-27.8 % normative olivine. These features resemble ultramafic rocks of restitic crustal rather than mantle origin. Such rocks probably crystallized at the base of a thickened arc-crust, as discussed below (cf. the Kohistan intra-oceanic arc, Yamamoto & Yoshino 1998). The micaceous xenolith consists of >95% biotite with Mg# 67. The mineral chemistry and associations are not appropriate for a mantle-derived glimmerite, and the bulk composition does not correspond to any normal sediment. Possible origins include: a residue from wet melting of pelite; hydrothermal or K-metasomatic alteration of mafic rock; or pre-metamorphic degradation and leaching of mafic volcanic material (cf. Moore and Waters, 1990).

GEOCHRONOLOGY

Biotite separates from the host dyke were dated by $^{40}Ar/^{39}Ar$ laser single-grain fusion method at the National Taiwan University. Mineral separates were extracted from the sample by handpicking and subsequently irradiated together with the LP-6 biotite standards (Odin *et al.*

1982) in the VT-C position for 30 hours at the THOR reactor. After irradiation, standards were totally fused using double-vacuum resistant furnace and samples were incrementally heated using a US LASER Nd-YAG laser operated in a continuous mode by changing laser output energy. The gas was analyzed by a VG 3600 mass spectrometer. Detailed analytical procedures are given by Lo *et al.* (2002). The analytical results are given in Table 4 and are plotted on the isotope correlation diagram of $^{39}Ar/^{40}Ar$ vs $^{36}Ar/^{40}Ar$ which gives an intercept age of 12.7 ± 0.1 (1σ) Ma with mean square of weighted deviates (MSWD) = 1.6 (Fig. 3a).

In-situ U-(Th-)Pb laser ablation MC-ICP-MS dating of zircons and monazites in polished thin sections were performed on three of the xenoliths at the NERC Isotope Geosciences Laboratory using Nu-Plasma HR and Thermo-Elemental Axiom MC-ICP-MS. The grains were ablated using a New Wave Research UP193SS Nd:YAG laser ablation system, using 20- or 35-μm-diameter spot or 20-μm-wide line raster, depending on the size of the crystal. Measurement procedures were conducted following Horstwood et al. (2003) with that for monazite modified to include an additional magnet jump to allow collection of ^{232}Th. Hardware parameters for the Nu Plasma illustrating collection of U-Pb data are detailed in Simonetti et al. (2005). The collected data were reduced and errors propagated using an in-house spreadsheet calculation package. For zircons, each age reported here represents the weighted mean of concordant clustered 206Pb/238U ages obtained from individual zircons. For monazites, owing to the presence of excess ^{206}Pb arising from *in-situ* decay of ^{230}Th, only the unaffected $^{208}Pb/^{232}Th$ ages are reported here. Analytical data are plotted in Fig. 3b-f and tabulated in Table 5 & 6.

In the felsic granulite sample (GCT-158g), most data define a discordia with a 504 ± 12 (2σ) Ma upper intercept (MSWD = 1.4) (Fig. 3b). If only the youngest three data points are considered, the weighted mean $^{206}Pb/^{238}U$ age is 16.8 ± 0.9 Ma (MSWD = 0.12), and we interpret this to be the best estimate of the young end member. Together with the zoning pattern shown in the BSE images (Fig. 3b), these data are interpreted to represent a two-component mixture of Cambrian igneous (cores or entire grains) and Middle Miocene metamorphic components (mostly rims). Zircons in the ultramafic xenolith (GCT-158p) occur as inclusions or along grain boundary zones. These grains do not exhibit any zoning in their BSE images and most grains form a sub-concordant cluster of data with a weighted mean $^{206}Pb/^{238}U$ age of 84.6 ± 4.6 Ma (MSWD = 0.63) (Fig. 3c). One grain has a younger weighted mean $^{206}Pb/^{238}U$ age of 15.6 ± 0.6 Ma (MSWD = 0.10) (Fig. 3d). These ages suggest the rock has a Late Cretaceous protolith component and experienced zircon growth during peak metamorphism in the Middle Miocene. The zircons from the micaceous xenolith (GCT-158a) are zoned. Apart from a discordant grain core with a $^{206}Pb/^{238}U$ age of 727 Ma, most data form a sub-concordant cluster around 400-474 Ma (Fig. 3e). The interpretation of the age of this rock is complex. At least two age components are inferred to exist: Proterozoic and ca. 450 Ma, with some data points representing a mixing of these components plus Pb loss and/or zircon growth at ca. 450 Ma and/or recently. Monazites from the same sample yield much younger ages, and three out of four analyses yielded a weighted mean age of $^{208}Pb/^{232}Th$ age of 14.4 ± 0.4 Ma with MSWD = 0.18 (Fig. 3f).

DISCUSSION

The composition and structure of the lower crust beneath southern Tibet remain unknown, but could comprise any of three units: (1) underthrust Indian plate lower crust, composed mainly of Early Proterozoic-Archean granulites; (2) subducted Indian passive margin sequence and Tethyan oceanic rocks, comprising Precambrian-Cretaceous sediments and trapped remnants of Mesozoic ophiolites, island arcs or (3) thickened Lhasa terrane lower crust, consisting of presumed Precambrian basement, Gangdese and Linzizong magmatic arc rocks. The U-Th-Pb ages obtained from this study provide new constraints on these hypotheses. The presence of ca. 85 Ma zircons in the ultramafic xenolith demonstrates that the rocks are unlikely to be dominated by Indian plate material, in which magmatic rocks of that age are absent. In contrast, these zircon ages are comparable with the Late Cretaceous-early Paleogene (120-49 Ma) Trans-Himalayan Gangdese magmatic arc. Moreover, recent isotopic evidence from mid-Miocene dykes emplaced south of the Yarlung-Tsangpo suture (King et al. 2007) indicates that Asian crust existed at depth to the south of the study area by the time of xenolith sampling. These zircon ages could also be compared with the Kohistan intra-oceanic arc in Pakistan, which contains 82-99 Ma mafic and ultramafic rocks and formed above a north-dipping intra-oceanic subduction zone of Neo-Tethys (Schaltegger et al. 2002). If so, this requires part of such an arc to have been accreted during northward subduction beneath southern Tibet prior to the India-Asia collision. The ca. 504 Ma zircons in the felsic granulites and the Late Ordovician-Early Devonian zircons with Proterozoic inheritance in the micaceous xenolith do not place any further constraints on the protolith origins as magmatic or metamorphic rocks of these ages occur in both Indian and Asian crust. For example, Precambrian basement rocks have been recovered in Amdo along the Bangong-Nujiang suture (Guynn et al. 2006). Detrital zircons of similar age were found in the Great Himalaya Sequence and Tethyan succession (DeCelles et al. 2000). Nevertheless, our results suggest that the lower crust of the southern Lhasa terrane attained peak granulite-facies metamorphism during ca. 17-14 Ma, shortly predating the timing of entrainment in the ultra-potassic dyke and transport to the surface.

The xenoliths can be compared with other suites sampled by volcanic rocks of different ages (0.5 to 28 Ma) distributed across Tibet (Fig. 1) and westward into the Pamirs, most of which also indicate a metamorphic crystallisation a few Ma before entrainment. The xenoliths of this study were extracted during ultrapotassic magmatism at ~13 Ma from crustal levels of 50-80 km along a well-constrained geotherm of 16°C/km. By 13 Ma, therefore, part of the lower crust of the southern Lhasa terrane was represented by hot and dry tonalitic mafic and felsic granulites and ultramafic rocks perhaps with a minor component of supracrustal material. The xenolith suite described from 28 Ma Na-rich calc-alkaline lavas in the southern Qiangtang terrane by Ding et al. (2007) is similarly dominated by meta-igneous mafic granulites, although these appear to define a hotter geotherm passing through ca. 980 °C at a maximum depth of around 45 km. In the Pamir, 11 Ma year old ultrapotassic lavas intruding the southern margin of the westernmost Qiangtang terrane (Ducea et al. 2003, Hacker et al. 2005) contain a suite of meta-igneous eclogitic and granulitic xenoliths that recrystallized mainly at conditions of 1000-1100 °C and 23-28 kbar, on a cooler geotherm of 10-12 °C/km. In contrast, however, a suite of xenoliths described from a 3 Ma old ultrapotassic dyke in the northern Qiangtang terrane of north-central Tibet (Hacker et al. 2000) show that the lower crust there is occupied by anhydrous meta-sedimentary granulite facies rocks that equilibrated at 800-1100 °C on a hot geotherm at depths of 30-50 km (Hacker et al. 2000). Still further north, mafic granulitic xenoliths that attained peak metamorphic conditions of 1000-1100 °C at depths of 50-60 km have also been recovered from 0.5 Ma shoshonitic lavas in the northern Songpan-Ganze terrane (Jolivet et al. 2003). In summary, the xenoliths of southern Tibet coupled with other lower crustal xenolith information described above support a two-part crustal structure model for Tibet and the Pamir (Schwab et al. 2004; Hacker et al. 2005). A crystalline basement extends from the southern Lhasa terrane to the southern Qiantang terrane with a possible western extension to the Pamir. Beyond this zone, the lower crust is occupied mainly by meta-sedimentary rocks at least up to the northern Qiangtang terrane.

The southern margin of the Asian plate is dominated by an extensive calc-alkaline batholith – the Gangdese granitoids with associated sub-aerial andesitic extrusives (Linzizong Formation). A major regional unconformity across southern Tibet has been documented with gently dipping Palaeocene Linzizong volcanics above folded mid-Upper Cretaceous Takena Formation red-beds, showing that significant crustal thickening occurred prior to the India-Asia collision (England & Searle 1986; Kapp et al. 2007; Leier et al. 2007). Given the geology of south Tibet, it is likely that the southern margin of Asia was similar to an Andean-type margin, both in crustal thickness and elevation during that time. The exact thickness of the crust of the margin by the time of collision is unclear, but could be around 60 km. This suggests the basement of the southern Lhasa terrane only thickened from 60 km in the Eocene to 75-80 km by ca. 17-14 Ma and has remained unchanged until the present day. By corollary, the thickened basement could have allowed the southern Lhasa terrane to reach its present elevation by ca. 17-14 Ma, consistent with other palaeoaltimetry estimates (Spicer et al. 2003, Rowley & Currie 2006). The xenolith temperature estimations indicate that a geothermal gradient of 16 °C/km prevailed during ca.17-14 Ma. This elevated geothermal gradient together with the widespread occurrence of ultrapotassic and adakitic volcanics in southern Tibet (e.g. Chung et al. 2005) indicate that the ambient temperature of the lower crust and upper mantle experienced a major thermal perturbation. Models for convective removal of thickened lithospheric mantle (England & Houseman, 1986; Turner et al., 1993), slab break-off (Maheo et al., 2002) and intracontinental subduction (Arnaud et al. 1992) could potentially explain the heat advection in the mantle. All these models emphasize the importance of heating from the underlying asthenosphere. Alternatively, the xenolith geotherm, which is less extreme than that recorded by xenolith suites further north, may reflect the culmination of crustal thickening in southern Lhasa terrane by that time, in which case the heat may have been derived from crustal radioactivity without input from the underlying mantle lithosphere (McKenzie & Priestley 2007).

ACKOWLEDGMENTS

We thank V. Pashley, N. Charnley and P. Jackson for sample preparation and analysis. G. Chan has been funded by a Croucher Foundation Scholarship. This work was supported by HKU CRCG and the Research Grants Council of the Hong Kong Special Administrative Region, China (HKU 7001/04P) to J. Aitchison. Isotope work at NIGL was funded by NERC (NIGFSC project 20427). The earliest version of the manuscript benefited from the comments of Simon Harley, Bradley Hacker and Lothar Ratschbacher. Tom Argles and an anonymous reviewer are thanked for their insightful comments.

Figure captions

Figure 1. a) Map of the Tibetan Plateau, showing sample location, terranes, sutures, major faults and distribution of Cenozoic magmatism. YS = Yarlung-Tsangpo suture zone; BS, Bangong-Nujiang suture; JS = Jinsha suture; KS = Kunlun suture, modified after Ding et al. (2007); other xenolith localities indicated as D-07: Yibuchaka (Ding et al. 2007); H-00: Taipinghu volcanic field (Hacker et al. 2000); J-03: Jingyu, Kunlun fault zone (Jolivet et al. 2003); H-05: arrow points towards location of Dunkeldik pipes in the Pamir range at ca. 37°40'N, 75°E (Ducea et al. 2003, Hacker et al. 2005). b) Map showing the xenolith-bearing ultrapotassic dyke cutting Xigaze flysch to the immediate north of the Yarlung-Tsangpo suture zone. Modified after Wang et al. (1984) and own observation.

Figure 2. Calculated thermobarometry for the studied xenoliths. Grey lines for partially constrained samples 158a, 158g and 158p, in which P-T conditions are determined by

intersection between geothermometer equilibria and the. linear geotherm defined by the remaining samples.

Figure 3. a) $^{36}Ar/^{40}Ar$ – $^{39}Ar/^{40}Ar$ isotope correlation diagram for the biotite separates from the xenolith bearing dyke (errors given in the figure are at 1 σ); b-f) Back-scattered electron images of representative zircon and monazite from the analysed samples (uniform scale bar is 50 μm) and concordia diagrams (b, c, e & f) and $^{206}Pb/^{238}U$ weighted average diagram (d). All errors given in figure are at 2σ. Analyses include laser ablation spots in cores and at tips of individual crystals. See text for details.

References

Arnaud, N.O., Vidal, P., Tapponnier, P., Matte, P. & Deng, W.M. 1992. The high K_2O volcanism of northwestern Tibet: geochemistry and tectonic implications. *Earth and Planetary Science Letters*, **111**, 351–367.

Chung, S.-L., Chu, M.-F., Zhang, Y., Xie, Y., Lo, C.-H., Lee, T.-Y., Lan, C.-Y., Li, X., Zhang, Q. & Wang, Y. 2005. Tibetan tectonic evolution inferred from spatial and temporal variations in post-collisional magmatism. *Earth-Science Reviews*, **68**, 173-196.

DeCelles, P.G., Gehrels, G.E., Quade, J., LaReau, B. & Spurlin, M. 2000. Tectonic implications of U/Pb zircon ages of the Himalayan orogenic belt in Nepal. *Science*, **288**, 497-499.

Ding, L., Kapp, P., Yue, Y. & Lai, Q. 2007. Postcollisional calc-alkaline lavas and xenoliths from the southern Qiangtang terrane, central Tibet. *Earth and Planetary Science Letters*, **254**, 28-389.

Ducea, M. N., Lutkov, V., Minaev, V. T., Ratschbacher, L., Luffi, P., Schwab, M., Gehrels, G.E., McWiliams, M., Vervoort, J. & Metcalf, J. 2003. Building the Pamirs: The view from the underside, *Geology*, **31**, 849-852.

England, P. & Searle, M.P. 1986. The Cretaceous - Tertiary deformation of the Lhasa block and its implications for the crustal thickening in Tibet. *Tectonics*, **5**, 1-14.

England, P. & Houseman, G. 1986. Finite strain calculations of continental deformation:2. Comparison with the India-Asia collision zone. *Journal of Geophysical Research*, **91**, 3664-3676.

Fettes, D. & Desmons, J. (Eds.) 2007. *Metamorphic Rocks: A Classification and Glossary of Terms*. Cambridge University Press, Cambridge, 256p.

Fuhrman, M.L. & Lindsley, D.H. 1988. Ternary-feldspar modeling and thermometry: *American Mineralogist*, **73**, 201-215.

Guynn, H., Kapp, Pullen, A., Heizler, M., Gehrels, G. & Ding, L. 2006. Tibetan basement rocks near Amdo reveal “missing” Mesozoic tectonism along the Bangong suture, central Tibet. *Geology*, **34**, 505-508.

Hacker, B., Gnos, E., Ratschbacher, L., Grove, M., McWilliams, Sobolev, S, Wan, J. & Wu, Z. 2000. Hot and dry deep crustal xenoliths from Tibet. *Science*, **287**, 2463-2466.

Hacker, B., Luffi, R., Lutkov, V., Minaev, V., Ratschbacher, L., Plank, T., Ducea, M., Patino-Douce, A., McWilliams, M. & Metcalf, J. 2005. Near-ultrahigh pressure processing of continental crust: Miocene crustal xenoliths from the Pamir. *Journal of Petrology*, **46**, 1661-1687.

Hauck, M.L., Nelson, K.D., Brown, L.D., Zhao, W. & Ross, A.R. 1998. Crustal structure of the Himalayan orogen at ~90° east longitude from Project INDEPTH deep reflection profiles. *Tectonics*, **17**, 481-500.

Holdaway, M. J. 2000. Application of new experimental and garnet Margules data to the garnet-biotite thermometer. *American Mineralogist*, **85**, 881-892.

Horstwood, M.S.A., Foster, G.I., Parrish, R.R., Noble, S.R. & Nowell, G.M. 2003. Common-Pb corrected in-situ U-Pb accessory mineral geochronology by LA-MC-ICP-MS: *Journal of Analytical Atomic Spectrometry*, **18**, 837-846.

Jolivet, M., Brunel, M., Seward, D., Xu, Z., Yang, J., Malavieille, J., Roger, F., Leyreloup, A., Arnaud, N. & Wu, C. 2003. Neogene extension and volcanism in the Kunlun Fault Zone, northern Tibet: New constraints on the age of the Kunlun Fault. *Tectonics*, **22**, 1052.

Kapp, P., DeCelles, P.G., Leier, A.L., Fabijanic, J.M., He, S., Pullen, A., Gehrels, G.E. & Ding, L. 2007. The Gangdese retroarc thrust belt revealed. *GSA Today*, **17**, 4-9.

King, J., Harris, N., Argles, T., Parrish, R., Charlier, B., Sherlock, S. & Zhang, H. F., 2007. First field evidence of southward ductile flow of Asian crust beneath southern Tibet. *Geology*, **35**(8), 727-730.

Leier, A. L., DeCelles, P.G., Kapp, P. & Ling, D.. 2007. The Takena Formation of the Lhasa terrane, southern Tibet: The record of a Late Cretaceous retroarc foreland basin. *Geological Society of America Bulletin*, **119**, 31-48.

Lo, C.-H., Chung, S.-L., Lee, T.-Y. & Wu, G.-Y. 2002. Age of the Emeishan flood magmatism and relations to Permian-Triassic boundary events. *Earth and Planetary Science Letters*, **198**, 449-458.

Maheo, G., Gullot, S., Blichert-Toft, J., Rolland, Y. & Pecher, A. 2002. A slab breakoff model for the Neogene thermal evolution of Southern Karakoram and South Tibet. *Earth and Planetary Science Letters*, **195**, 45-58.

McKenzie, D. & Priestley, K. 2008. The influence of lithospheric thickness variations on continental evolution. *Lithos*, **102**, 1-11.

Moore, J. M. and Waters, D. J. 1990. Geochemistry and origin of cordierite - orthoamphibole/orthopyroxene - phlogopite rocks from Namaqualand, South Africa. *Chemical Geology*, **85**, 77-100.

Nelson, K.D., Zhao, W., Brown, L.D. et al. 1996. Partially molten middle crust beneath southern Tibet: synthesis of project INDEPTH results. *Science*, **274**, 1684-1695.

O'Brien, P.J. & Rotzler, J. 2003. High-pressure granulites: formation, recovery of peak conditions and implications for tectonics. *Journal of Metamorphic Geology*, **21**, 3-20.

Odin, G.S. et al. 1982. Interlaboratory standards for dating purposes, *In*: Odin, G. S. (ed.) *Numerical Dating in Stratigraphy*, Wiley, Chichester, 123-149.

Owens, T.J. & Zandt, G. 1997. Implications of crustal property variations for models of Tibetan plateau evolution. *Nature*, **387**, 37-43.

Powell, R. 1985. Regression diagnostics and robust regression in geothermometer/geobarometer calibration: The garnet-clinopyroxene thermometer revisited. *Journal of Metamorphic Geology*, **3**, 327-342.

Powell, R. & Holland, T.J.B. 1988. An internally consistent dataset with uncertainities and correlations: Applications to geobarometry, worked examples and a computer program. *Journal of Metamorphic Geology*, **6**, 173-204.

Rowley, D. B. & Currie, B. S., 2006. Palaeo-altimetry of the late Eocene to Miocene Lunpola basin, central Tibet. *Nature*, **439**(7077), 677-681.

Schaltegger, U., Zeilinger, G., Frank, M. & Burg, J.-P. 2002. Multiple mantle sources during island arc magmatism: U-Pb and Hf isotopic evidence from the Kohistan arc complex, Pakistan. *Terra Nova*, **14**, 461-468.

Schulte-Pelkum, V., Monsalve, G., Sheehan, A. Pandey, M.R., Sapkota, S., Bilham, R. & Wu, F. 2005. Imaging the Indian subcontinent beneath the Himalaya. *Nature,* **435**, 1222-1225.

Schwab, M., Ratschbacher, L., Siebel, W., McWilliams, M., Lutkov, V., Minaev, F., Chen, K., Stanek, K., Nelson, B., Frisch, W. & Wooden, J. 2004. Assemblage of the Pamirs: Age and origin of magmatic belts from the southern Tien Shan to the southern Pamirs and their relation to Tibet. *Tectonics*, **23**, TC4002.

Simonetti, A., Heaman, L.M., Hartlaub, R.P., Creaser, R.A., MacHattie, T.G. & Bohm, C. 2005. U-Pb zircon dating by laser ablation-MC-ICP-MS using a new multiple ion counting Faraday collector array. *Journal of analytical atomic spectrometry*, **20**, 677-686.

Spicer, R. A., Harris, N. B. W., Widdowson, M., Herman, A. B., Guo, S. X., Valdes, P. J., Wolfe, J. A. & Kelley, S. P., 2003. Constant elevation of southern Tibet over the past 15 million years. *Nature*, **421**(6923), 622-624.

Tilmann, F.J., J. Ni, and the INDEPTH III Seismic Team. 2003. Seismic imaging of the downwelling Indian lithosphere beneath Central Tibet. *Science*, **300**, 1424-1427.

Turner, S., Hawkesworth, C., Liu, J., Rogers, N., Kelley, S. & Van Calsteren, P. 1993. Timing of Tibetan uplift constrained by analysis of volcanic rocks. *Natur*e, **364**, 50-53.

Wang, X.B., Xiao, X.C., Cao, Y.G. & Zheng, H.X. 1984. Geological map of the ophiolite zone along the middle Yarlung Zangbo (Tsangpo River), Xizang (Tibet): Academy of the Geological Sciences, Beijing.

Yamamoto, H. & Yoshino, T. 1998. Superposition of replacements in the mafic granulites of the Jijal complex of the Kohistan arc, northern Pakistan: dehydration and rehydration within deep arc crust. *Lithos*, **43**, 219-234.

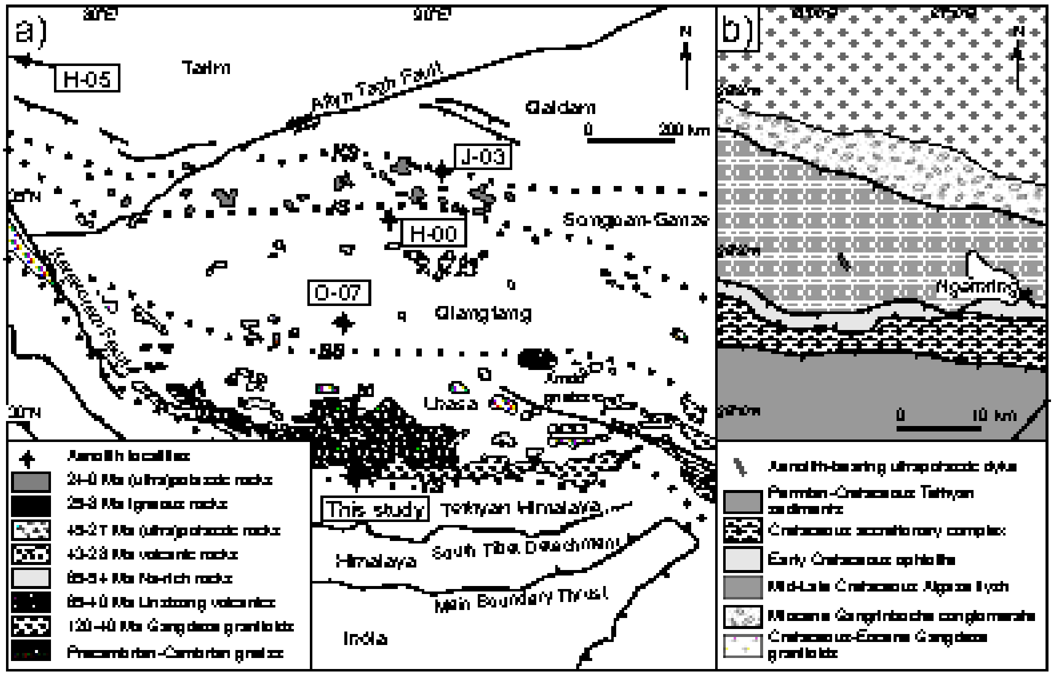

a)
H-05
Tarim
Altyn Tagh Fault
Qaidam
0
200 km
N
J-03
H-00
Songpan-Ganze
O-07
Qiangtang
Lhasa
This study
Tethyan Himalaya
Himalaya
South Tibet Detachment
Main Boundary Thrust
India
Karakoram Fault
Xenolith localities
24-0 Ma (ultra)potassic rocks
25-8 Ma Igneous rocks
45-27 Ma (ultra)potassic rocks
43-23 Ma volcanic rocks
65-54 Ma Na-rich rocks
65-40 Ma Linzizong volcanics
120-40 Ma Gangdese granitoids
Precambrian-Cambrian gneiss
b)
N
Ngamring
0
10 km
Xenolith-bearing ultrapotassic dyke
Permian-Cretaceous Tethyan sediments
Cretaceous accretionary complex
Early Cretaceous ophiolite
Mid-Late Cretaceous Xigaze flysch
Miocene Gangrinboche conglomerate
Cretaceous-Eocene Gangdese granitoids

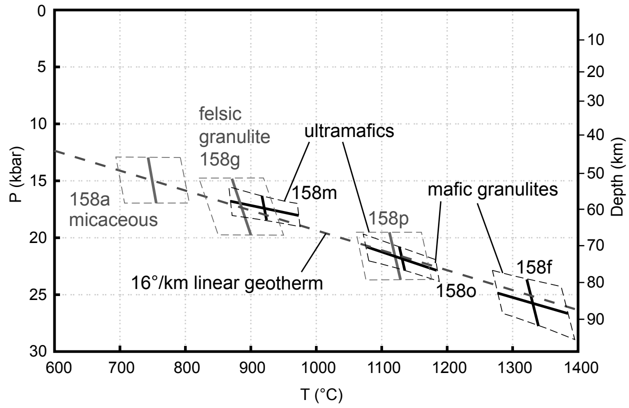

P (kbar)
Depth (km)
T (°C)
felsic
granulite
158g
ultramafics
158m
158a
micaceous
mafic granulites
158p
158f
158o
16°/km linear geotherm

Figure 2.

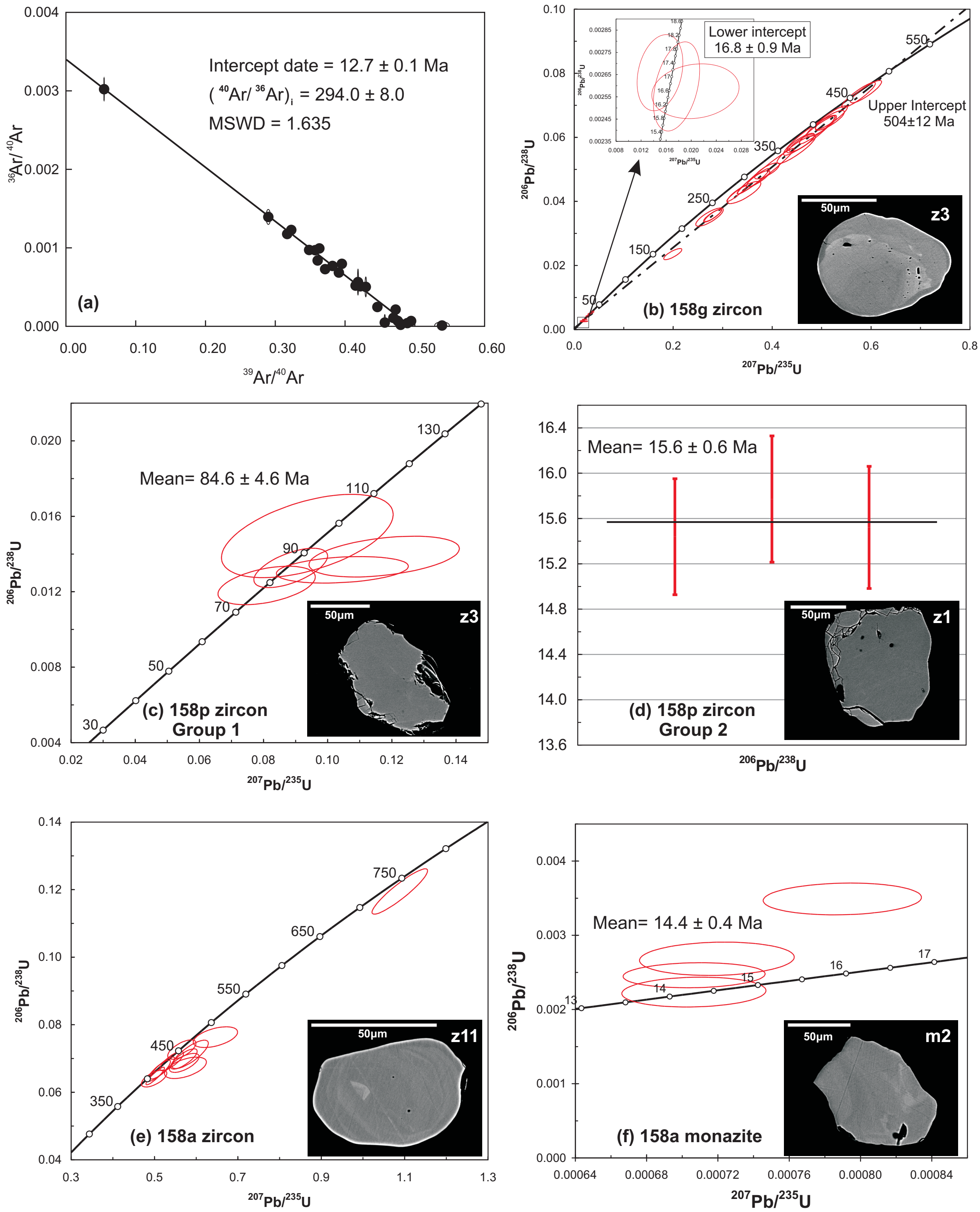

Intercept date = 12.7 ± 0.1 Ma
(^{40}Ar/^{36}Ar)$_i$ = 294.0 ± 8.0
MSWD = 1.635
(a)
^{36}Ar/^{40}Ar
^{39}Ar/^{40}Ar
Lower intercept
16.8 ± 0.9 Ma
Upper Intercept
504±12 Ma
(b) 158g zircon
z3
50µm
^{206}Pb/^{238}U
^{207}Pb/^{235}U
Mean= 84.6 ± 4.6 Ma
(c) 158p zircon
Group 1
Mean= 15.6 ± 0.6 Ma
(d) 158p zircon
Group 2
z1
(e) 158a zircon
z11
Mean= 14.4 ± 0.4 Ma
(f) 158a monazite
m2

Table 6. LA-MC-ICPMS monazite data

Sample	Analysis	^{204}Pb (mV)	^{206}Pb (mV)	^{208}Pb (mV)	^{232}Th (mV)	^{238}U (mV)	Th[a] (ppm)	Th/U[b]	Common-Pb corrected isotopic ratios					Common-Pb corrected ages (Ma)			
									f206[C] %	^{206}Pb/^{238}U	2σ %	^{208}Pb/^{232}Th	2σ %	^{206}Pb/^{238}U	2σ	^{208}Pb/^{232}Th	2σ
158a																	
m10_1	core	0.006	1.5	10.1	2546.92	184.69	38939	25.4	6.71	0.0035	5.0	0.000790	4.6	22.5	1.1	16.0	0.7
m2_1	rim	0.011	1.4	9.5	2731.45	239.26	41760	21.0	12.45	0.0022	7.3	0.000707	4.7	14.4	1.1	14.3	0.7
m3_1	rim	0.008	1.7	10.8	3104.35	299.71	47462	19.0	8.41	0.0027	6.8	0.000719	4.9	17.3	1.2	14.5	0.7
m4_1	rim	0.008	1.8	10.8	3157.30	340.61	48271	17.0	7.90	0.0025	5.6	0.000707	4.6	15.9	0.9	14.3	0.7

Notes

[a]Accuracy of Th content is ~20%

[b]Normalized to Th/U ratio of the standard

[C]Common ^{206}Pb expressed as a percentage of total ^{206}Pb measured

[d]Isotopic ratios are corrected for common-Pb. Common-Pb correction based on a two-stage model (Stacey and Kramers, 1975) and the interpreted age of the crystal

Table 2 Thermobarometry calculations

Sample	Rock Type	T(°C)	method	P (kbar)	method
158a	micaceous xenolith	740-755	Grt-Bt, Holdaway 2000, calibration 5AV	13-17	assumed
158f	mafic granulite	1330 ± 50	Grt-Cpx, Powell 1985	25.8 ± 1.9	THERMOCALC, $a\,H_2O$=0.5[a]
158g	felsic granulite	870-900	Two-feldspar, Fuhrman & Lindsley 1988	15-20	assumed
158m	ultramafic xenolith	920 ± 50	Grt-Cpx, Powell 1985	17.4 ± 1.0	THERMOCALC, CaTs excluded[b], $a\,H_2O$=0.5[a]
158o	mafic granulite	1130 ± 50	Grt-Cpx, Powell 1985	21.9 ± 0.9	THERMOCALC, CaTs excluded[b]
158p	ultramafic xenolith	1110-1130	Grt-Cpx, Powell 1985	19-24	assumed

[a] H_2O activity was set at 0.5
[b] Calcium Tschermaks (CaTs) end member was excluded from THERMOCALC calculation

Table 4: Results of $^{40}Ar/^{39}Ar$ laser single-grain fusion experiments

No.	Atmos.(%)	$^{36}Ar/^{39}Ar$	$^{37}Ar/^{39}Ar$	$^{38}Ar/^{39}Ar$	$^{40}Ar/^{39}Ar$	$^{40}Ar/^{36}Ar$	Date (Ma)
1	2.05	.14629E-03	.20520E-02	.58100E-01	.21317E+01	.14572E+05	12.9 ± .2
2	.57	.40119E-04	.36107E-03	.55360E-01	.21137E+01	.52684E+05	13.0 ± .1
3	89.28	.55335E-01	.36624E+00	.51492E-01	.18313E+02	.33095E+03	12.3 ± 4.8
4	23.54	.20145E-02	.94554E-04	.57934E-01	.25576E+01	.12696E+04	12.1 ± .1
5	22.74	.20174E-02	.11312E-01	.45500E-01	.26466E+01	.13119E+04	12.6 ± .3
6	1.21	.84008E-04	.24194E-03	.41655E-01	.20725E+01	.24671E+05	12.6 ± .2
7	.31	.19622E-04	.20183E-03	.37899E-01	.18841E+01	.96021E+05	11.6 ± .3
8	20.24	.17544E-02	.12506E-01	.50395E-01	.25855E+01	.14737E+04	12.7 ± .1
9	24.79	.23261E-02	.19340E-03	.46673E-01	.28010E+01	.12042E+04	13.0 ± .2
10	21.53	.19614E-02	.16673E-03	.47391E-01	.27210E+01	.13873E+04	13.2 ± .2
11	6.31	.45217E-03	.27590E-03	.44643E-01	.21453E+01	.47443E+04	12.4 ± .3
12	2.01	.13768E-03	.23602E-03	.58268E-01	.20502E+01	.14891E+05	12.4 ± .1
13	34.76	.37100E-02	.18851E-03	.52264E-01	.31826E+01	.85784E+03	12.9 ± .1
14	41.19	.48098E-02	.15811E-01	.52889E-01	.34767E+01	.72285E+03	12.7 ± .6
15	36.29	.38062E-02	.10490E-01	.52036E-01	.31257E+01	.82121E+03	12.3 ± .2
16	7.28	.55391E-03	.78873E-02	.47137E-01	.22692E+01	.40967E+04	13.0 ± .3
17	1.42	.10547E-03	.84372E-03	.46334E-01	.22172E+01	.21023E+05	13.5 ± .4
18	28.75	.27918E-02	.15263E-03	.48484E-01	.28979E+01	.10380E+04	12.8 ± .1
19	15.08	.12092E-02	.14781E-03	.46319E-01	.23984E+01	.19835E+04	12.6 ± .1
20	3.18	.22977E-03	.30636E-03	.44426E-01	.21598E+01	.94000E+04	12.9 ± .2
21	15.34	.12562E-02	.22745E-01	.38733E-01	.24379E+01	.19407E+04	12.8 ± .3
22	14.85	.11707E-02	.47757E-02	.45889E-01	.23558E+01	.20124E+04	12.4 ± .5
23	28.67	.27161E-02	.21850E-03	.49493E-01	.28282E+01	.10413E+04	12.5 ± .3
24	29.34	.27337E-02	.23459E-03	.47997E-01	.27823E+01	.10178E+04	12.2 ± .2
25	16.67	.13477E-02	.55132E-03	.40361E-01	.24179E+01	.17941E+04	12.4 ± .7

J-value = .00347774 ± 0.00001195
Total Gas Age = 12.6 ± 0.1 Ma
Mean Age = 12.6 STDEV = 0.4Ma

Note:
J-value: Weighted mean of three fusions of irradiation standard LP-6 biotite standards (Odin *et al.* 1982)
The date is obtained by using the following equations:

$$\text{Date} = \frac{1}{\lambda}\ln\left(1 + J\frac{^{40}Ar*}{^{39}Ar_K}\right), \text{ and}$$

$$\frac{^{40}Ar*}{^{39}Ar_K} = \frac{\left[^{40}Ar/^{39}Ar\right]_m - 295.5\left[^{36}Ar/^{39}Ar\right]_m + 295.5\left[^{36}Ar/^{37}Ar\right]_{Ca}\left[^{37}Ar/^{39}Ar\right]_m}{1 - \left[^{39}Ar/^{37}Ar\right]_{Ca}\left[^{37}Ar/^{39}Ar\right]_m} - \left[\frac{^{40}Ar}{^{39}Ar}\right]_K$$

where $[\ ]_{Ca}$ and $[\ ]_K$ = isotope ratios of argon extracted from irradiated calcium and potassium salts (values cited in the text) and $[\ ]_m$ = isotope ratio of argon extracted from irradiated unknown.

Date (Ma) = the date calculated using the following decay constants: $\lambda_\varepsilon = 0.581\text{x}10^{-10}\text{yr}^{-1}$; $\lambda_\beta = 4.962\text{x}10^{-10}\ \text{yr}^{-1}$; $\lambda = 5.543 \times 10^{-10}\ \text{yr}^{-1}$; $^{40}K/K = 0.01167$ atom % (Steiger and Jäger, 1977).

The quoted error is one standard deviation and does not include the error in the standard error, or the error in the interference corrections.

Table 1. Mineral analyses used in pressure-temperature estimations

Sample	158a	158a	158f	158f	158f	158f	158f	158g	158g	158g	158m	158m	158m	158m	158m	158o	158o	158o	158p	158p	158p	158p
Mineral	Grt	Bt	Grt	Cpx	Pl	Am	Bt	Kfs	Pl	Grt	Grt	Cpx	Pl	Am	Bt	Grt	Cpx	Pl	Grt	Cpx	Am	Bt
Location	core	mean	mean	mean	mean	mean	mean	mean	mean	mean	mean	core	mean	mean	mean	mean	core	mean	mean	core	mean	mean
SiO_2	39.38	36.72	40.21	50.89	61.67	40.57	38.78	65.22	62.47	39.43	39.50	51.64	58.66	38.60	36.88	39.17	51.31	62.79	39.67	50.46	42.02	38.09
TiO_2	0.00	4.80	0.06	0.65	0.01	1.92	3.26	0.12	0.00	0.11	0.09	0.56	0.06	2.60	4.54	0.09	0.66	0.04	0.12	1.06	2.81	5.16
Al_2O_3	22.67	18.41	22.61	10.39	24.44	16.30	17.79	19.98	23.93	22.42	22.46	9.43	27.21	18.59	15.53	22.02	9.02	22.96	22.28	8.71	15.85	16.99
FeO	27.22	12.81	18.62	8.63	0.21	12.02	10.81	0.02	0.06	20.71	18.84	5.63	0.39	8.96	13.09	20.93	8.62	0.14	21.64	10.26	12.34	11.85
MnO	0.40	0.04	0.26	<0.03	<0.02	<0.04	<0.05	nd	<0.01	0.28	0.30	<0.05	<0.02	<0.02	0.07	0.42	<0.05	<0.02	0.50	0.19	<0.03	<0.02
MgO	9.28	14.50	11.14	9.49	nd	11.78	19.63	<0.03	nd	9.51	6.49	10.85	<0.02	12.44	16.01	8.84	9.45	0.00	8.54	10.58	11.46	14.87
CaO	2.99	0.10	8.79	17.70	5.36	10.07	0.17	0.79	4.90	8.34	14.01	20.01	8.34	11.73	0.07	9.22	17.79	4.02	9.02	16.45	9.72	0.08
Na_2O	0.18	0.34	0.07	3.41	7.54	2.68	0.51	3.40	7.38	<0.05	0.11	2.52	6.97	1.30	0.41	nd	2.97	7.40	nd	2.47	2.74	0.41
K_2O	nd	9.46	<0.01	<0.01	1.50	2.52	7.67	11.96	2.16	0.02	<0.01	<0.02	0.06	3.16	9.19	<0.01	0.04	2.10	<0.01	0.18	2.31	9.17
F		0.32				0.25	0.68							0.58	0.89						0.14	0.40
Cl		0.08				0.91	0.17							0.04	0.06						0.12	0.11
Sum	102.12	97.59	101.76	101.15	100.72	99.01	99.47	101.47	100.88	100.82	101.79	100.64	101.68	97.99	96.75	100.68	99.87	99.45	101.77	100.35	99.51	97.14
Oxygens	12	22	12	6	8	23	22	8	8	12	12	6	8	23	22	12	6	8	12	6	23	22
Si	2.969	5.313	2.971	1.852	2.729	5.935	5.406	2.935	2.760	2.968	2.968	1.871	2.584	5.669	5.436	2.968	1.889	2.803	2.978	1.863	6.104	5.498
Ti	0.000	0.522	0.003	0.018	0.000	0.212	0.342	0.004	0.000	0.006	0.005	0.015	0.002	0.287	0.503	0.005	0.018	0.001	0.007	0.029	0.307	0.559
Al	2.014	3.141	1.970	0.446	1.275	2.811	2.922	1.060	1.246	1.989	1.989	0.403	1.413	3.218	2.697	1.967	0.392	1.209	1.971	0.379	2.715	2.892
Fe	1.716	1.551	1.151	0.263	0.008	1.471	1.261	0.001	0.002	1.303	1.184	0.171	0.014	1.101	1.615	1.326	0.266	0.005	1.358	0.317	1.499	1.432
Mn	0.025	0.005	0.016	0.001	0.001	0.004	0.006	0.000	0.000	0.018	0.019	0.002	0.000	0.002	0.008	0.027	0.001	0.001	0.032	0.006	0.004	0.002
Mg	1.042	3.126	1.227	0.515	0.000	2.568	4.078	0.002	0.000	1.066	0.727	0.586	0.001	2.723	3.518	0.999	0.518	0.000	0.955	0.582	2.480	3.201
Ca	0.242	0.015	0.696	0.690	0.254	1.578	0.026	0.038	0.232	0.673	1.128	0.777	0.393	1.847	0.011	0.749	0.702	0.192	0.725	0.651	1.514	0.013
Na	0.027	0.096	0.010	0.240	0.647	0.761	0.138	0.297	0.632	0.007	0.016	0.177	0.595	0.370	0.118	0.000	0.212	0.641	0.000	0.177	0.773	0.115
K	0.000	1.746	0.001	0.000	0.084	0.470	1.364	0.686	0.121	0.002	0.000	0.001	0.003	0.593	1.728	0.001	0.002	0.120	0.001	0.009	0.429	1.687
Sum	8.035	15.515	8.045	4.025	4.999	15.809	15.542	5.023	4.994	8.032	8.036	4.001	5.006	15.810	15.634	8.041	4.001	4.972	8.027	4.011	15.824	15.398
F		0.147				0.116	0.300							0.267	0.415						0.107	0.183
Cl		0.019				0.226	0.040							0.009	0.016						0.090	0.027

nd: not determined

Table 5 LA-MC-ICPMS zircon data

Sample	Analysis	^{204}Pb (mV)	^{206}Pb (mV)	^{207}Pb (mV)	^{238}U (mV)	U (ppm)[a]	Isotopic ratios[b] $^{207}Pb/^{206}Pb$	2σ %	$^{206}Pb/^{238}U$	2σ %	$^{207}Pb/^{235}U$	2σ %	Rho	Ages (Ma) $^{207}Pb/^{206}Pb$	2σ	$^{206}Pb/^{238}U$	2σ	$^{207}Pb/^{235}U$	2σ
158a																			
z11-1	core	N/A	6.86	0.39	65	434	0.0661	2.0	0.1195	4.6	1.0884	5.0	0.92	809.1	41.7	727.4	35.3	747.7	53.9
z11-2	rim	0.000	3.19	0.17	55	371	0.0620	6.0	0.0672	3.9	0.5743	7.2	0.54	672.4	129.0	419.5	16.7	460.8	40.9
z17-1	rim	N/A	2.52	0.13	41	277	0.0603	3.8	0.0687	3.3	0.5713	5.1	0.66	615.1	82.3	428.3	14.8	458.9	29.0
z17-2	rim	N/A	14.57	0.71	256	1713	0.0561	1.6	0.0648	3.3	0.5016	3.6	0.90	457.5	34.5	404.8	13.7	412.8	18.3
z17-3	core	N/A	2.41	0.13	36	239	0.0614	5.9	0.0763	3.3	0.6461	6.7	0.49	653.3	126.0	474.1	16.1	506.1	43.2
z16-1c	rim	N/A	6.00	0.29	99	666	0.0560	2.3	0.0672	4.0	0.5190	4.6	0.86	453.4	51.6	419.1	17.2	424.5	24.0
z16-2	rim	N/A	5.70	0.28	94	627	0.0567	2.6	0.0692	3.4	0.5413	4.3	0.79	479.6	57.9	431.6	15.0	439.3	23.2
z16-3c	rim	N/A	6.15	0.30	104	696	0.0558	2.3	0.0664	3.9	0.5103	4.5	0.86	442.9	51.2	414.3	16.5	418.6	23.1
z15-1	core	N/A	2.48	0.12	44	296	0.0565	3.9	0.0641	3.2	0.4989	5.0	0.63	471.3	85.9	400.3	13.1	411.0	25.1
z15-3	rim	N/A	2.72	0.14	43	287	0.0565	3.7	0.0726	3.2	0.5656	4.9	0.66	470.6	82.2	452.1	15.1	455.1	27.9
158g																			
z2-1b	rim	N/A	1.64	0.08	49	327	0.0565	5.0	0.0351	6.6	0.2735	8.3	0.80	472.9	111.2	222.4	15.0	245.5	22.9
z2-1c	core	0.007	3.52	0.17	59	396	0.0568	3.2	0.0606	8.4	0.4749	9.0	0.93	485.2	70.4	379.3	32.6	394.6	42.3
z3-1b	core	N/A	3.47	0.17	72	483	0.0571	3.2	0.0495	4.2	0.3898	5.2	0.79	494.7	70.7	311.6	13.2	334.2	20.6
z3-1c	core	0.005	1.87	0.09	46	306	0.0582	4.8	0.0428	6.6	0.3431	8.1	0.81	536.1	104.0	270.1	18.2	299.5	28.0
z3-2b	rim	N/A	3.40	0.18	151	1015	0.0613	4.5	0.0236	6.0	0.1992	7.5	0.80	651.2	95.7	150.1	9.2	184.4	15.1
z3-2c	rim	0.002	4.58	0.22	133	893	0.0570	2.7	0.0355	4.5	0.2791	5.2	0.86	492.2	59.0	224.9	10.3	250.0	14.7
z3-3b	rim	N/A	5.48	0.26	162	1084	0.0571	2.4	0.0357	4.5	0.2809	5.1	0.88	495.6	53.8	226.0	10.3	251.4	14.5
z3-3c	rim	N/A	5.88	0.28	135	908	0.0567	2.3	0.0463	7.0	0.3620	7.4	0.95	479.8	51.6	291.8	20.8	313.7	26.7
z5-1b	rim	0.000	0.25	0.01	88	589	0.0493	15.9	0.0026	6.3	0.0177	17.1	0.37	162.7	371.2	16.7	1.1	17.8	3.1
z5-2a	core	0.000	0.62	0.02	150	1007	0.0474	10.5	0.0042	5.9	0.0272	12.0	0.49	69.1	249.4	26.8	1.6	27.2	3.3
z6-2c	homog.	0.004	0.25	0.01	86	579	0.0410	19.2	0.0027	5.3	0.0150	19.9	0.26	-290.0	489.0	17.1	0.9	15.1	3.0
z6-4b	homog.	0.007	0.18	0.01	65	435	0.0582	27.2	0.0026	3.9	0.0207	27.5	0.14	538.3	595.8	16.6	0.6	20.8	5.8
z7-1b	core	0.000	5.43	0.26	78	525	0.0571	2.5	0.0635	4.3	0.5000	5.0	0.87	494.5	54.5	397.1	17.7	411.7	25.0
z7-1c	core	N/A	7.56	0.36	94	630	0.0569	2.0	0.0732	4.4	0.5747	4.8	0.91	488.9	44.1	455.5	20.8	461.0	27.9
z7-2	rim	0.001	4.61	0.22	90	600	0.0568	2.7	0.0494	11.9	0.3872	12.2	0.98	485.3	59.3	310.9	37.7	332.3	46.7
z7-3	rim	0.001	4.46	0.22	89	598	0.0573	2.7	0.0471	4.4	0.3720	5.2	0.85	501.8	59.9	296.8	13.3	321.1	19.3
z7-4b	core	N/A	7.72	0.37	113	759	0.0572	2.0	0.0623	5.7	0.4915	6.1	0.94	498.9	44.8	389.8	22.9	406.0	29.8
z7-4c	core	N/A	7.37	0.36	90	606	0.0576	2.1	0.0743	3.9	0.5899	4.4	0.88	514.9	45.2	461.8	18.4	470.8	25.8
z8-1	core	N/A	5.67	0.27	78	526	0.0570	2.4	0.0662	4.6	0.5198	5.1	0.89	490.1	52.2	413.1	19.5	425.0	26.8
z8-2c	core	N/A	5.73	0.28	90	600	0.0573	2.4	0.0582	3.8	0.4598	4.5	0.85	501.5	52.2	365.0	14.4	384.1	20.8
z8-3	core	0.002	5.12	0.25	71	475	0.0574	2.5	0.0653	3.9	0.5168	4.6	0.84	507.4	55.5	407.7	16.4	423.0	24.1
z8-4	rim	0.002	3.62	0.18	59	393	0.0579	3.1	0.0562	6.4	0.4489	7.1	0.90	526.3	67.3	352.6	23.1	376.5	31.8
z8-5b	rim	0.002	4.49	0.22	72	483	0.0570	2.8	0.0582	4.3	0.4576	5.1	0.84	491.5	61.0	364.8	15.9	382.6	23.3
z9-1c	core	N/A	0.23	0.01	76	509	0.0479	19.7	0.0032	1.9	0.0209	19.8	0.09	93.7	467.3	20.4	0.4	21.0	4.2
z10-1	core	N/A	10.83	0.51	236	1582	0.0561	1.7	0.0424	4.7	0.3283	5.0	0.94	457.4	36.8	267.8	12.8	288.3	16.4
z10-2	rim	N/A	1.22	0.05	209	1398	0.0483	6.5	0.0054	4.8	0.0361	8.1	0.60	112.2	153.0	34.9	1.7	36.0	3.0
z10-3	rim	N/A	1.12	0.04	208	1396	0.0457	7.2	0.0049	4.0	0.0311	8.2	0.48	-17.6	173.5	31.7	1.3	31.1	2.6
158p																			
z1-1b	homog.	N/A	0.04	0.00	23	140	N/A	N/A	0.0024	3.3	N/A	N/A	N/A	N/A	N/A	15.4	0.5	N/A	N/A
z1-2b	homog.	N/A	0.05	0.00	25	152	N/A	N/A	0.0024	3.5	N/A	N/A	N/A	N/A	N/A	15.8	0.6	N/A	N/A
z1-3b	homog.	N/A	0.06	0.00	33	203	N/A	N/A	0.0024	3.5	N/A	N/A	N/A	N/A	N/A	15.5	0.5	N/A	N/A
z3-1b	homog.	N/A	0.26	0.01	26	157	0.0576	15.5	0.0132	4.4	0.1046	16.1	0.27	515.8	340.1	84.3	3.7	101.0	16.9
z5-1c	homog.	N/A	0.23	0.01	20	124	0.0615	15.0	0.0139	6.4	0.1176	16.3	0.39	657.7	321.7	88.8	5.7	112.9	19.3
z7-1b	core	0.000	0.35	0.01	34	207	0.0476	13.8	0.0123	6.8	0.0810	15.3	0.44	80.2	326.5	79.0	5.4	79.1	12.5
z7-2b	core	0.001	0.78	0.03	71	434	0.0484	8.5	0.0133	6.4	0.0885	10.6	0.61	118.3	199.2	84.9	5.5	86.1	9.5
z6-2a	homog.	0.001	0.19	0.01	16	97	0.0454	20.0	0.0150	12.1	0.0937	23.3	0.52	-33.1	484.6	95.7	11.6	90.9	22.0

[a]Accuracy of U content is ~20%

[b]All isotopic ratios are not common-Pb corrected

homog. = structureless zircon, no zoning

Table 3 Calculated bulk rock compositions (in wt%) and normative mineral contents

Sample	158a	158f	158g	158m	158o	158p
Rock Type	micaceous xenolith	mafic granulite	felsic granulite	ultramafic xenolith	mafic granulite	ultramafic xenolith
SiO_2	37.9	57.8	74.1	45.6	66.5	43.6
TiO_2	4.8	0.3	0.0	2.0	0.1	1.7
Al_2O_3	19.0	18.0	14.3	16.9	17.3	15.4
FeO	13.5	5.3	1.4	9.4	3.4	13.9
MnO	0.1	0.0	0.0	0.1	0.1	0.2
MgO	14.8	4.4	0.6	8.7	1.8	10.8
CaO	0.2	8.8	2.2	13.2	4.9	11.4
Na_2O	0.3	4.6	3.1	2.1	4.7	1.1
K_2O	9.4	0.8	4.2	1.8	1.3	1.9
Forced sum	100.0	100.0	100.0	100.0	100.0	100.0
Mg#	52.3	45.3	31.4	48.1	34.7	43.6
Q	0.0	2.3	33.3	0.0	19.1	0.0
Ab	0.8	39.8	26.6	1.9	40.4	0.0
An	0.0	25.1	10.4	31.5	21.7	31.5
Or	0.0	4.9	25.0	10.4	7.5	9.8
Ne	1.6	0.0	0.0	8.6	0.0	5.1
Lc	41.9	0.0	0.0	0.0	0.0	0.9
C	8.1	0.0	0.7	0.0	0.0	0.0
Di	0.0	14.3	0.0	27.5	1.3	20.5
Hy	0.0	12.6	3.9	0.0	9.6	0.0
Ol	37.5	0.0	0.0	15.4	0.0	27.8
Il	9.2	0.5	0.1	3.8	0.2	3.3
Mt	1.1	0.4	0.1	0.8	0.3	1.1